Available online at www.sciencedirect.com
ScienceDirect
Geochimica et Cosmochimica Acta 73 (2009) 6937–6951
Geochimica et Cosmochimica Acta
www.elsevier.com/locate/gca

# Molecular dynamics studies of $CaAl_2Si_2O_8$ liquid. Part II: Equation of state and a thermodynamic model

Mark S. Ghiorso [a,*], Dean Nevins [b], Ian Cutler [b], Frank J. Spera [b]

[a] OFM-Research Inc., 7336 24th Ave. NE, Seattle, WA 98115, USA
[b] Department of Earth Science & Institute for Crustal Studies, University of California, Santa Barbara, CA 93106, USA

Received 25 February 2009; accepted in revised form 13 August 2009; available online 23 August 2009

**Abstract**

A thermodynamic model and equation of state (EOS) is developed from the molecular dynamics simulation experiments of Spera et al. (2009) for $CaAl_2Si_2O_8$ liquid over the temperature range 3500–6000 K and pressure interval 0–125 GPa. The model is constructed utilizing the isothermal Universal EOS of Vinet et al. (1986) combined with an expression for the temperature-dependence of the internal energy derived from density functional theory (Rosenfeld and Tarazona, 1998). It is demonstrated that this model is more successful at reproducing the data than the temperature-dependent Universal EOS (Vinet et al., 1987) or the volume-explicit EOS of Ghiorso (2004a). Distinct parameterizations are required to model low (<20 GPa) and high (>20 GPa) pressure regimes. This result is ascribed to the affect of liquid structure on macroscopic thermodynamic properties, specifically the interdependence of average cation-oxygen coordination number on the bulk modulus. The thermodynamic transition between the high- and low-pressure parameterizations is modeled as second order, although the nature of the transition is open to question and may well be first order or lambda-like in character.

Analysis of the thermodynamic model reveals a predicted region of liquid–liquid un-mixing at low-temperatures (<1624 K) and pressures (<1.257 GPa). These pressure–temperature conditions are above the glass transition temperature but within the metastable liquid region. They represent the highest temperatures yet suggested for liquid–liquid un-mixing in a silicate bulk composition. A shock wave Hugoniot curve is calculated for comparison with the experimental data of Rigden et al. (1989) and of Asimow and Ahrens (2008). The comparison suggests that the model developed in this paper underestimates the density of the liquid by roughly 10% at pressures greater than ~20 GPa.


## 1. INTRODUCTION

The objective of this paper is to demonstrate how the molecular dynamics simulations reported in Spera et al. (2009, hereafter Part I) may be utilized to develop a thermodynamic model of $CaAl_2Si_2O_8$-composition liquid. The data set reported in Part I represents conditions at which the internal energy ($E$) and the volume ($V$, or density, $\rho$) of the liquid are known at a given temperature ($T$) and pressure ($P$). In order to construct this data set, Molecular Dynamics computations where performed utilizing the microcanonical ensemble to generate 72 state points along isochors that cover the pressure range 0–125 GPa. Energies were chosen to yield temperatures between 3500 and 6000 K at approximately 500 K intervals.

The exercise of calibrating an equation of state (EOS) and thermodynamic model for $CaAl_2Si_2O_8$ liquid over such a broad temperature and pressure range highlights some important considerations in modeling homogeneous materials that undergo significant changes in melt structure with $T$ and $P$. In minerals and other crystalline solids, structural variation is often addressed by formulating a model with parameters that characterize the internal structural state of the material, and the equilibrium configuration is determined for specified $T$ and $P$ by computation of homogeneous equilibrium (Thompson, 1969, 1970). Often, the

* Corresponding author. Tel.: +1 206 550 1850.
*E-mail address:* ghiorso@ofm-research.org (M.S. Ghiorso).

0016-7037/$ - see front matter © 2009 Elsevier Ltd. All rights reserved.
doi:10.1016/j.gca.2009.08.012

structural variation is constrained by crystallographic symmetry and the formalism of Landau's theory (Tolédano and Tolédano, 1987) is applicable. In amorphous materials, polymer models (Flory, 1988) and associated solution theory are often utilized to accommodate the energetic consequences of temperature-, pressure- and compositionally-dependent structural variation. An example of the latter theory applied to molten $SiO_2$ is given in Ghiorso (2004a). In aqueous solutions, accounting for structural variability is intrinsic to the very successful method of describing their thermodynamic properties in terms of ions and associated ionic complexes. In all these cases, structural variation with $T$ and $P$ is important because such variation affects the entropy of the material, and one cannot hope to model the energy of a system at finite temperature with any veracity in the absence of a physical description of the system's entropy.

The molecular dynamics simulations reported in Part I demonstrate that $CaAl_2Si_2O_8$ liquid undergoes significant changes in melt structure as a function of pressure. This is illustrated in Figs. 5 and 7 of Part I, which summarize data on the dependence of oxygen coordination number (CN) with pressure along a nominal 3500 and 6000 K isotherm, respectively. For example, in Fig. 5 (Part I) the fraction of Si at 3500 K in nearest neighbor coordination with four oxygen atoms ($SiO^{[4]}$)[1], five oxygen atoms ($SiO^{[5]}$), etc., are plotted along with the average CN of Si as a function of pressure. The trends in $SiO^{[n]}$ are very similar to those found for $AlO^{[n]}$ and reflect a regular and smooth increase in the radius ratio of the cation with respect to oxygen induced by increasing pressure. To first order, the changes in average CN of Si and Al are a good measure of the *macroscopic* volume of the liquid. This relation is shown in Fig. 1, where average coordination number of O about Si ($SiO^{[\bar{n}]}$) computed from 72 simulations performed along 12 isochors is plotted as a function of the specific volume. Fig. 1 establishes that there is a relation between the structure of $CaAl_2Si_2O_8$ liquid and the volumetric properties of the system. Closer inspection indicates some important second order features of this relation. The first six low-specific volume (high-pressure) isochors define a linear trend that is distinct from another that characterizes the high-specific volume (low-pressure) simulations. While the underlying cause for these two distinct trends may lie in the observation that the low-pressure group is dominated by $(Si,Al)O^{[4]}$ and $(Si,Al)O^{[5]}$ and the high-pressure group by $(Si,Al)O^{[5]}$ and $(Si,Al)O^{[6+]}$ (Figs. 5 and 7, Part I), there is a more abrupt shift in CN of Ca and a marked change in the coordination number of O about O that better differentiates the two groupings. The local environment of Ca and O reveals that a significant reorganization of the structure of $CaAl_2Si_2O_8$ liquid takes place across this interval, and whether the consequence of this structural change is a phase transition of pseudo-first order character or a displacive transition that spans several GPa, the inescapable conclusion is that the thermodynamic properties of the liquid on either side of the interval need not be related, any more than the properties of one polymorph of a mineral need be related to another. In particular, these observations suggest that a single EOS (or thermodynamic model) parameterization will be insufficient to describe the data set of Part I. We expect, for example, that quite different values of the bulk modulus ($K$) will be required to account for the potentially different compression mechanisms in the low- and high-pressure regimes and that this will also be true for the thermal expansivity ($\alpha$) and the Grüneisen parameter ($\gamma$). Experimental work on the solution of Ar in molten $CaAl_2Si_2O_8$ at pressure (Bouhifd and Jephcoat, 2006; Bouhifd et al., 2008) demonstrates that there is a rapid change in solubility mechanism in the range 15–20 GPa, which lends support to our inference of phase transition like behavior in the liquid.

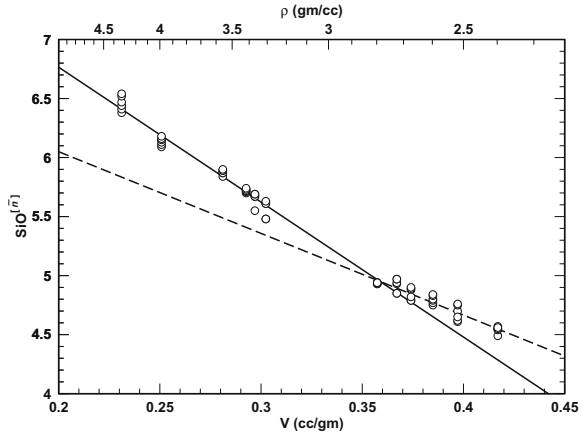


Fig. 1. Average nearest neighbor coordination number of oxygen about silicon (Ave $SiO^{[\bar{n}]}$) plotted against specific volume (and density) for the 72 MD state points of Part I. The solid line is a linear regression of data from the high-pressure isochors, while the dashed line represents the same through the low-pressure data.

We begin this paper by analyzing the observations of Part I in terms of the Universal EOS of Vinet et al. (1986, 1987, 1989) and then compare these solutions to those obtained using the EOS of Ghiorso (2004a). Finally, we develop an EOS and complete thermodynamic model for $CaAl_2Si_2O_8$ liquid using the potential energy approximation of Rosenfeld and Tarazona (1998) in combination with the temperature independent version of the Universal EOS (Vinet et al., 1986). This combined model is used in the last section of the paper to examine the liquid–liquid un-mixing in molten $CaAl_2Si_2O_8$ and to compute a theoretical shock Hugoniot.

## 2. PRELIMINARY EOS ANALYSIS

The Universal EOS of Vinet et al. (1986) is a pressure explicit equation of state that has been found to be reliable for a wide variety of compounds to extreme values of compression. The Universal EOS has a simple form,

$$P = \frac{3K(1-x)e^{\eta(1-x)}}{x^2} \tag{1}$$

[1] We adopt the following notation, $AB^{[n]}$, which denotes that there are $n$ atoms of "B" in nearest neighbor coordination with atom "A".

where $\eta = \frac{3}{2}(K' - 1)$ and $x = (\frac{V}{V_0})^{1/3}$. The three parameters of the EOS, $V_0$, $K$, and $K'$, are the zero pressure volume, *isothermal* bulk modulus, and the pressure derivative of the *isothermal* bulk modulus, for some reference temperature ($T_r$). While the Universal EOS does not incorporate explicit provision for pressure-induced variation in the structure of the material, it offers a convenient parameterization and a starting point for examining the data set of Part I.

Table 1
Universal EOS fits to isotherms.

| Isotherm ($K$) | Sum-of-squares | $V_0$ | $K$ | $K'$ |
|---|---|---|---|---|
| 3500-low $P$ | 0.06 | 0.451601 | 7.405233 | 8.554065 |
| 3500-high $P$ | 3.62 | 0.367461 | 47.40261 | 7.210359 |
| **3500** | **32.28** | **0.433122** | **9.926412** | **9.87999** |
| 4000-low $P$ | 0.062 | 0.449172 | 10.1497 | 7.663792 |
| 4000-high $P$ | 1.57 | 0.380513 | 39.30513 | 7.327294 |
| **4000** | **16.09** | **0.440295** | **10.40354** | **9.470172** |
| 4500-low $P$ | 0.03 | 0.45673 | 9.560292 | 8.567842 |
| 4500-high $P$ | 0.86 | 0.40297 | 26.79937 | 7.802924 |
| **4500** | **4.78** | **0.452248** | **9.819279** | **9.265064** |
| 5000-low $P$ | 0.03 | 0.46294 | 10.00496 | 8.524746 |
| 5000-high $P$ | 0.696 | 0.408396 | 27.90265 | 7.480413 |
| **5000** | **3.82** | **0.457251** | **10.77817** | **8.849689** |
| 5500-low $P$ | 0.016 | 0.461078 | 14.11587 | 6.936002 |
| 5500-high $P$ | 0.305 | 0.415506 | 27.34356 | 7.340795 |
| **5500** | **3.04** | **0.466965** | **10.51567** | **8.677041** |
| 6000-low $P$ | 0.05 | 0.480659 | 9.740531 | 8.341857 |
| 6000-high $P$ | 0.194 | 0.433676 | 21.53198 | 7.568282 |
| **6000** | **1.41** | **0.476429** | **10.18755** | **8.553595** |

After organizing the simulation data of Part I by isotherm, we fitted them to the Universal EOS. Resulting parameter values are reported in Table 1. Model curves and residuals are displayed in Fig. 2. As anticipated, the Universal EOS fails to capture the second order features of $\rho(P)$ for this data set. Residuals form a distinct trend at low-pressure and are larger than the reported uncertainty at higher pressures (Fig. 2). This non-random pattern to model residuals can be eradicated by fitting the high- and low-pressure isochors separately, partitioning the data set of Part I according to a low-$P$ regime dominated by CaO[7] and OO[10–12] (Figs. 5 and 7, Part I) and a high-$P$ regime characterized by CaO[10–11] and OO[14–15]. Resulting fits are reported in Table 1. Examining the sum-of-squares of residuals ($SS_{res}$) of these fits and those for each complete isotherm, it is apparent that the statistical improvement in quality of the fit is significant. In addition, this exercise demonstrates that the low- and high-pressure regimes are modeled by different average isothermal bulk moduli, with a value of $10.16 \pm 2.18$ GPa extracted for the low-$P$ MD data and a value of $31.72 \pm 9.64$ for the high-$P$ data. The former value is in excellent agreement with the recent experimental study of Ai and Lange (2008).

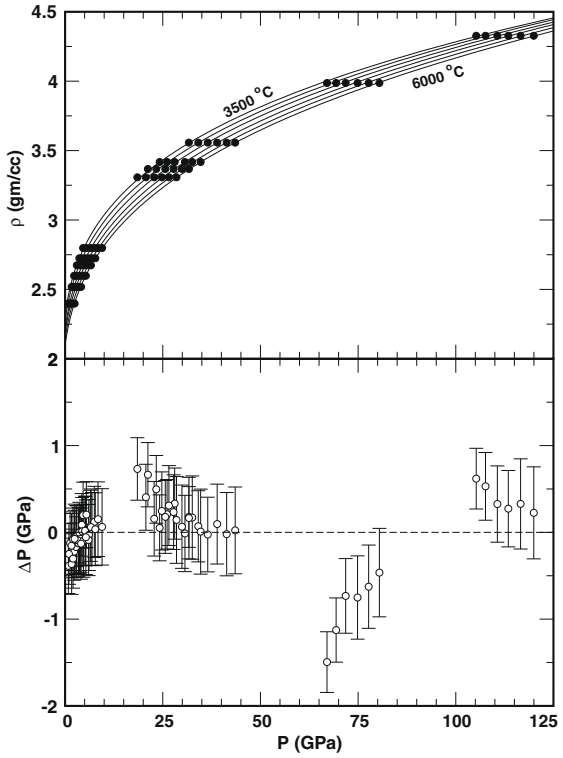


Fig. 2. Model isotherms and data residuals for fits to the Universal EOS (Vinet et al., 1986). Parameters are provided in Table 1. In the upper panel, the uncertainty in pressure for the MD data points is smaller than the size of the symbol. In the lower panel, the ordinate refers to the difference between the MD value (Part I) and the model value, and the brackets give the uncertainty estimated from the molecular dynamics simulation.

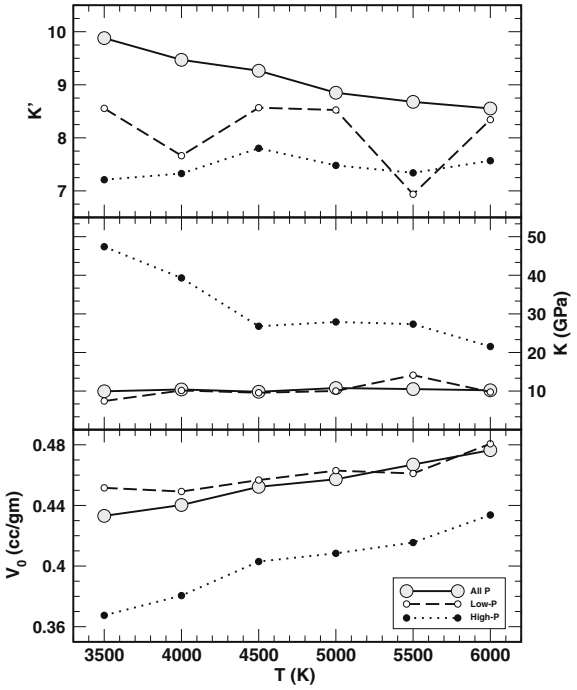


Fig. 3. Parameters of the Universal EOS of Vinet et al. (1986) calibrated from subsets of the data of Part I and plotted against temperature. Solid lines connect parameter values extracted from data along complete isotherms. The dashed lines show variation in parameters extracted from low-pressure isotherms, while the dotted lines connect high-pressure isotherm parameterizations. Numbers are from Table 1.

The Universal EOS parameter values for each isotherm are plotted in Fig. 3. The displayed trends suggest that it might be possible to construct a $P(V, T)$ equation by making the $V_0$, $K$, and $K'$ parameters functions of $T$. This approach is somewhat empirical, and Vinet et al. (1987) suggest that a better and more thermodynamically consistent formulation would be to include a "thermal pressure" correction to Eq. (1) as

$$P = \frac{3K(1-x)e^{\eta(1-x)}}{x^2} + \alpha K(T - T_r) \tag{2}$$

where $\alpha$ is the isobaric coefficient of thermal expansion at the reference temperature and pressure, which Vinet et al. (1987) suggest be modeled as a constant. Attempts to fit the entire Part I data set or just the low- and high-$P$ subsets with an EOS of the form of Eq. (2) fail because the fits do not capture the correct spacing of the isotherms at elevated pressure. This failure suggests that Eq. (2) does not adequately model the high-pressure thermal coefficient of expansion for this fluid.

As an alternative to expressing the Vinet EOS parameters of Table 1 as empirical functions of temperature, it is worth exploring other EOS formulations that are capable of reproducing the data set of Part I and for which the $T$-dependence has a more physical basis. One such EOS is that of Ghiorso (2004a), which is volume-explicit and has the form

$$V = \frac{V_{0,T} + (V_{1,T} + V_{0,T}a)(P - P_r) + \left(\frac{V_2}{2} + V_{1,T}a + V_{0,T}b\right)(P - P_r)^2}{1 + a(P - P_r) + b(P - P_r)^2} \tag{3}$$

This expression is based on a Taylor series expansion of the volume

$$V = V_{0,T} + V_{1,T}(P - P_r) + \frac{V_2}{2}(P - P_r)^2 + \frac{V_3}{6}(P - P_r)^3 + \frac{V_4}{24}(P - P_r)^4 \tag{4}$$

where the coefficients $V_{0,T}$, $V_{1,T}$, $V_2$, $V_3$, and $V_4$ are the zeroth through fourth order pressure derivatives of the volume at the reference pressure ($P_r$). Eq. (3) is obtained from Eq. (4) by a Padé transformation that generates the identities

$$a = \frac{V_2 V_3 - \frac{1}{2}V_{1,T}V_4}{2V_{1,T}V_3 - 3V_2^2} \tag{5}$$

$$b = \frac{\frac{1}{4}V_2 V_4 - \frac{1}{3}V_3^2}{2V_{1,T}V_3 - 3V_2^2} \tag{6}$$

The parameters $V_2$, $a$, and $b$ in Eq. (3) are taken to be temperature independent. The temperature-dependence of $V_{0,T}$ is given by

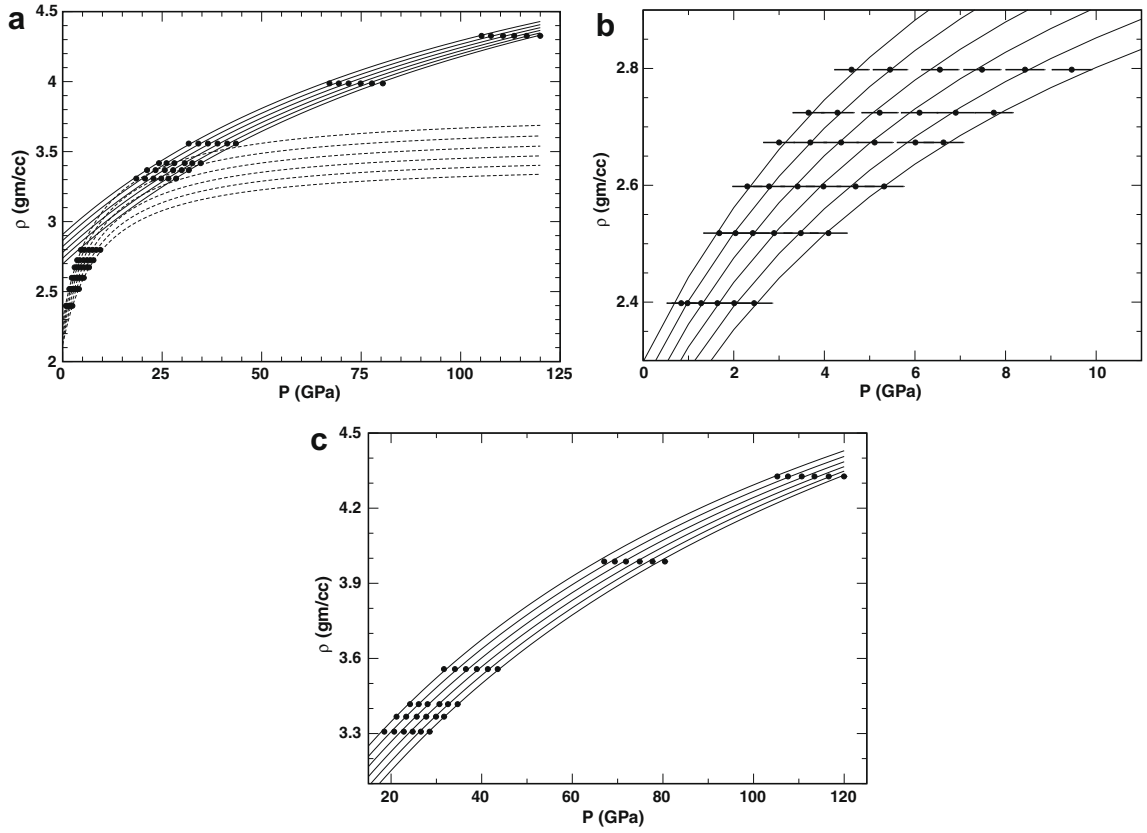


Fig. 4. Modeled densities computed from the volume-explicit EOS of Ghiorso (2004a) and the parameters of Table 2 compared to MD simulation data from Part I. (a) Dashed curves calculated from low-pressure parameterization, solid curves from high-pressure parameterization. See Table 2. Uncertainty in MD pressure estimates is within the size of the symbols. (b) Enlargement of the low-pressure regime. MD one sigma uncertainties in pressure estimates are from Part I. (c) Enlargement of the high-pressure regime. One sigma uncertainties in MD pressure estimates are approximately the size of the symbols.

$$V_{0,T} = V_{0,T_r} e^{\alpha(T-T_r)} \tag{7}$$

where $\alpha$ is a constant parameter corresponding to the isobaric thermal coefficient of expansion. $V_{1,T}$ is given by (Ghiorso and Kress, 2004)

$$V_{1,T} = -V_{0,T}^2 \left\{ \frac{1}{M\left[c_{T_r} + \frac{dc}{dT}(T-T_r)\right]^2} + \frac{T\alpha^2}{C_P} \right\} \tag{8}$$

where $C_P$ is the isobaric heat capacity, $M$ is the system mass, $c_{T_r}$ is the sound speed in the material at $T_r$, and $\frac{dc}{dT}$ is its temperature derivative. The EOS of Eq. (3) was constructed so that the temperature-dependence of its parameters [Eqs. (7) and (8)] could be inferred from measurable quantities. It has been applied successfully to experimental data on a wide variety of silicate liquids (Ghiorso, 2004b) and to molecular dynamics simulation data on molten $SiO_2$ (Ghiorso, 2004a).

Parameterizations of the EOS of Eq. (3) to the data from Part I are displayed in Fig. 4 with coefficients provided in Table 2. Taking the lead from the Universal EOS analysis, the data set is partitioned into low- and high-pressure subsets and each is fitted separately. The model recovers each subset of the data set to within the reported fluctuations in $P$ that are an intrinsic part of the Molecular Dynamics simulations. Further evaluation of the applicability of Eq. (3) requires examination of higher order volume derivatives and comparison of modeled values of $E$ with those of Part I.

The internal energy may be computed from Eq. (3) using the thermodynamic identity, $E = H - PV$, where $H$ is the enthalpy of the liquid, via

$$E = H_{T_r,P_r} + \int_{T_r}^{T} C_P dT + \int_{P_r}^{P} \left( V - T\frac{\partial V}{\partial T} \right) dP - PV \tag{9}$$

The parameters of Table 2 permit the evaluation of the last three terms of Eq. (9). Internally consistent values of the constant $H_{T_r,P_r}$ can be obtained from the MD results of Part I and are found to be $-153.073$ and $-152.918$ kJ/g, respectively, for the low- and high-pressure data sets. Recovery of the internal energy is demonstrated in Fig. 5. The analysis captures the essential features of the temperature and pressure dependence of the internal energy array, but residuals are larger than the estimates of uncertainty, which are in turn smaller than the plotted symbols (see figure legend).

Table 2
Parameter values for the EOS of Ghiorso (2004a).

| Parameter | Low-$P$ calibration | High-$P$ calibration |
|---|---|---|
| $V_{0,T_r}$ ($cm^3$/g) | 0.410148 | 0.325480 |
| $\alpha$ ($K^{-1}$) | $3.23905 \times 10^{-5}$ | $3.00631 \times 10^{-5}$ |
| $c_{T_r}$ (cm/s) | 2384.39 | 6420.66 |
| $\frac{dc}{dT}$ (cm/s K) | 0.0714161 | 0.0567792 |
| $C_P$ (J/g K)[a] | 1.52872 | 1.52872 |
| $V_2$ ($cm^3$/g $GPa^2$) | 0.0110032 | $-1.30792 \times 10^{-5}$ |
| $a$ ($GPa^{-1}$) | 0.851845 | 2.62529 |
| $b$ ($GPa^{-2}$) | 0.118737 | 0.0455112 |

$T_r = 5000$ K.
[a] Computed from the model of Lange and Navrotsky (1992).

In order to further investigate the advantages and disadvantages of this solution it is instructive to evaluate higher-order volumetric/temperature-derivative properties from the MD simulation data and compare these against model predictions. We choose to examine $(\frac{\partial P}{\partial T})_V$—$(=\alpha K)$ the "thermal pressure coefficient," $C_V$—the isochoric heat capacity $[\equiv (\frac{\partial E}{\partial T})_V]$, $K$, $\alpha$, and $\gamma$—the thermal Grüneisen parameter. $(\frac{\partial P}{\partial T})_V$ may be obtained from the MD simulation data of Part I by computing finite difference derivatives between ($P$, $T$)-state points determined along an isochore. Values are plotted in Fig. 6a along with uncertainty estimates obtained by formal error propagation (Bevington, 1969) on the assumption of uncorrelated errors in $T$ and $P$. Similarly, finite difference derivatives of ($E$, $T$)-state points along an isochore yield estimates of $C_V$, and values are plotted in Fig. 6c. Given that $K \equiv -V/(\frac{\partial V}{\partial P})_T$, $K$ may be estimated by computing finite difference derivatives of volume with respect to pressure between state points along an isotherm. These estimates and their associated uncertainties are plotted in Fig. 6b. Estimates of the remaining two quantities are obtained from their formal definitions: $\alpha = (\frac{\partial P}{\partial T})_V / K$ and $\gamma = \alpha K V / C_V$. Values and their associated uncertainties are plotted in Fig. 6d and e.

Model predictions of the thermal pressure coefficient and isochoric heat capacity agree well with MD estimates (Fig. 6a and b), although there is some mis-prediction of both quantities for the densest isochore. Prediction fails, however, for the bulk modulus at intermediate to elevated pressures (Fig. 6c). This misfit is a reflection of the fact that the slope of the model high-$P$ isotherms plotted in Fig. 4a is too shallow for $P \sim 25$ GPa and increasingly too steep for $P > 60$ GPa. The inability to successfully model the high-pressure bulk modulus carries over expectedly to the thermal coefficient of expansion (Fig. 6d), but is not reflected in the Grüneisen parameter, as model residuals in both $\alpha$ and $C_V$ tend to cancel each other.

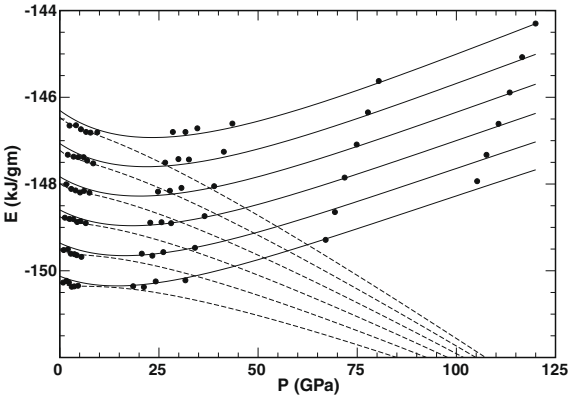


Fig. 5. Internal energy computed from the volume-explicit EOS of Ghiorso (2004a) and the parameters of Table 2 compared to MD simulation data from Part I. Dashed curves calculated from low-pressure parameterization, solid curves from high-pressure parameterization. Symbols are larger than estimated uncertainty in pressure.

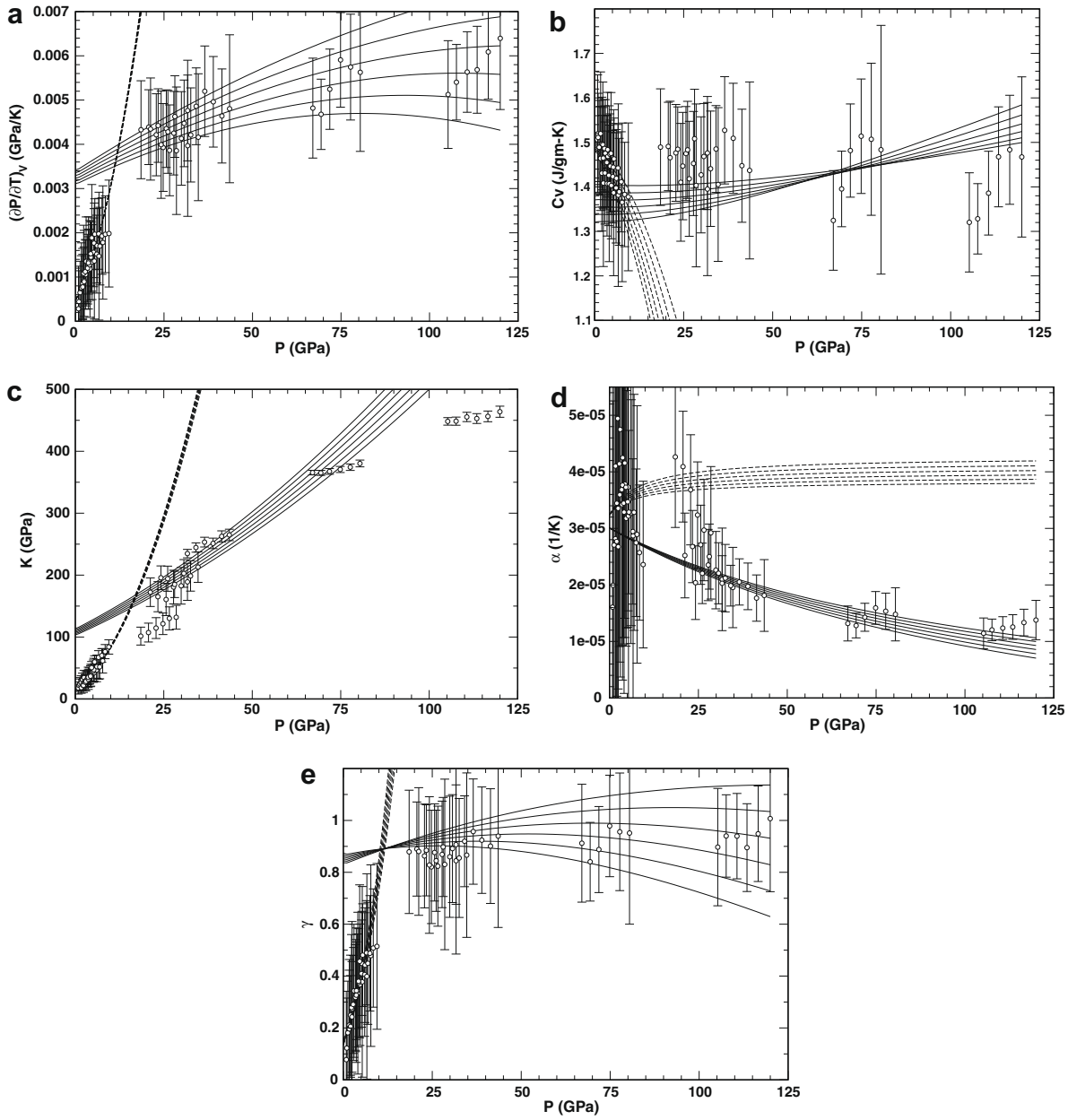


Fig. 6. Modeled derivative properties computed from the volume-explicit EOS of Ghiorso (2004a) and the parameters of Table 2 compared to MD simulation data from Part I. Dashed curves calculated from low-pressure parameterization, solid curves from high-pressure parameterization. Uncertainty in MD derived quantities are shown as $\pm 1\sigma$. (a) Thermal pressure coefficient, equivalent to $\alpha K$. (b) Isochoric heat capacity. (c) Bulk modulus. (d) Isobaric thermal coefficient of expansion. (e) Thermal Grüneisen coefficient.

In summary, the EOS embodied in Eq. (3) does an acceptable job in modeling *E–V–P–T* relations for the Part I data set, but it fails to capture important higher-order nuances of the data array. Furthermore, its successes depend on quite different parameterizations for the low- and high-*P* segments of the data set, and while this is not a flaw, it does bring to issue which branch of the model is applicable in the intermediate pressure regime and the practical matter of transitioning between model segments. In practice, one could compute the Gibbs free energy of the low- and high-*P* model liquids and find the locus of (*P, T*) points that define a "phase transition" between the two. In this context, however, inspection of Fig. 4a suggests that there will be a finite volume change along this transition curve (the isotherms for the low- and high-*P* model curves do not cross) and that implies a first order liquid–liquid phase transition. Before adopting a model with this sort of physical ramification it is important to establish that some less provocative formulation might not yield a model that fits the data equally well if not better.

Any thermodynamic model we formulate for $CaAl_2Si_2O_8$ liquid must acknowledge the dependence of

macroscopic bulk properties on microscopic structure (e.g. Figs. 4–7 in Part I), but if a model could be formulated that allows the transition between low- and high-$P$ structural regimes to be continuous, then such a model is clearly superior. In the next section, we develop such a model by combining a pressure explicit EOS with an expression for the internal energy derived from density functional theory.

## 3. PROPOSED EOS AND THERMODYNAMIC MODEL

In a seminal paper, Rosenfeld and Tarazona (1998) demonstrate that there is a general relation for the temperature and volume dependence of the potential energy ($U$) of dense classical fluids. The leading terms of this expression are

$$U(V,T) = a(V) + b(V)T^{3/5} \tag{10}$$

where $a(V)$ and $b(V)$ are unrestricted functions of volume. The MD simulations of Part I provide values of $U$ computed along 12 isochors, and these are plotted against corresponding values of $T^{3/5}$ in Fig. 7. Straight lines are fitted to these data as indicated in the upper panel of the figure; regression parameters and statistics are provided in Table 3. Residuals to these fits are plotted in the lower panel of Fig. 7. Eq. (10) does an excellent job representing the MD data for all but the two densest isochors. For these cases, the residuals form a parabolic pattern, suggesting

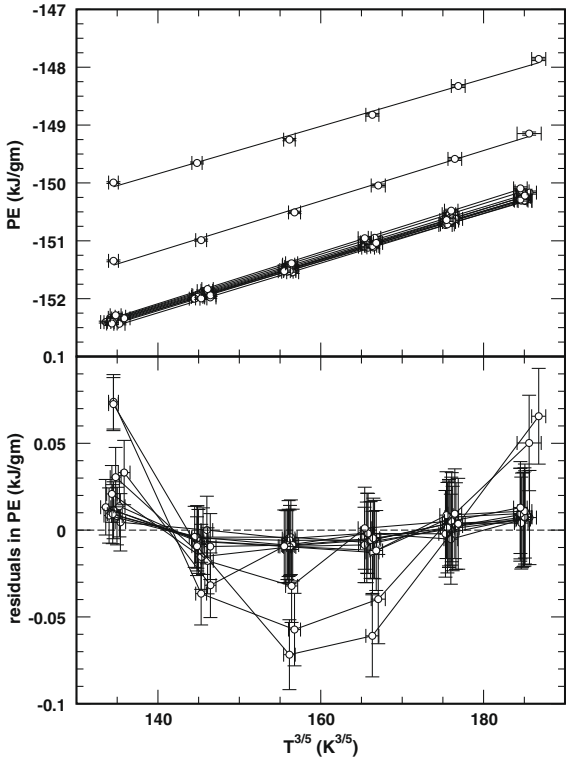


Fig. 7. Predicted trends and residuals for the model of Rosenfeld and Tarazona (1998) applied to estimates of the potential energy from Part I. Intercept and slope parameters as well as statistics related to the linear fits to the data (displayed in the upper panel) are reported in Table 3. Brackets indicate $\pm 1\sigma$ uncertainties.

perhaps the addition of a term involving $T^{6/5}$ to the model equation. In further developing the thermodynamic analysis in this paper, we will not pursue extension of Eq. (10) to higher order terms. At worst, this approximation will introduce an error ~0.05% in the modeled energy.

The internal energy of the system is given by the identity (Part I)

$$E(V,T) = U(V,T) + \frac{3n}{2}RT \tag{11}$$

where $n$ is the number of atoms in the formula unit of $CaAl_2Si_2O_8$ (i.e. 13), $R$ is the universal gas constant in units of energy/g K. Substitution of Eq. (10) into Eq. (11) gives a Rosenfeld–Tarazona compatible model expression for the internal energy

$$E(V,T) = a(V) + b(V)T^{3/5} + \frac{3n}{2}RT \tag{12}$$

Our first objective is to derive from Eq. (12) a Rosenfeld–Tarazona compatible EOS. To do so we follow the algorithm developed by Saika-Voivod et al. (2000). Using the definition,

$$A(V,T) = E(V,T) - TS(V,T) \tag{13}$$

of the Helmholtz free energy, a pressure explicit EOS may be obtained from the thermodynamic identity

$$P = -\left(\frac{\partial A}{\partial V}\right)_T \tag{14}$$

if an expression for the entropy of the system ($S$) is available. Fortunately, such an expression may be easily obtained. Start by writing the total derivative of $S(V,T)$ as

$$dS = \left(\frac{\partial S}{\partial T}\right)_V dT + \left(\frac{\partial S}{\partial V}\right)_T dV \tag{15}$$

The two partial derivatives in Eq. (15) may be rewritten using the first law of thermodynamics ($dE = TdS - PdV$) as

$$dS = \frac{1}{T}\left(\frac{\partial E}{\partial T}\right)_V dT + \left[\frac{1}{T}\left(\frac{\partial E}{\partial V}\right)_T + \frac{P(V,T)}{T}\right]dV \tag{16}$$

and this expression may be integrated along a path from some reference volume ($V_0$) and reference temperature ($T_0$) to $(V,T_0)$ and then from $(V,T_0)$ to $(V,T)$:

$$S(V,T) - S(V_0,T_0) = +\frac{1}{T_0}\int_{V_0}^{V}\left[\left(\frac{\partial E}{\partial V}\right)_T + P(V,T_0)\right]dV + \int_{T_0}^{T}\frac{1}{T}\left(\frac{\partial E}{\partial T}\right)_V dT \tag{17}$$

Substitution of Eq. (12) into Eq. (17) and carrying out the integrations results in a Rosenfeld–Tarazona compatible model expression for the entropy

$$S(V,T) = S(V_0,T_0) + \frac{1}{T_0}\left[a(V) + T_0^{3/5}b(V) - a(V_0) - T_0^{3/5}a(V_0) + \int_{V_0}^{V}P(T_0,V)dV\right] - \frac{3}{2}\left(\frac{1}{T^{2/5}} - \frac{1}{T_0^{2/5}}\right)b(V) + \frac{3n}{2}R\ln\left(\frac{T}{T_0}\right) \tag{18}$$

Table 3
Rosenfeld and Tarazona (1998) fits to potential energy.

| Volume (g/cm$^3$) | $U = a + bT^{3/5}$ | | | | | |
|---|---|---|---|---|---|---|
| | $a$ | SE $a$ | $b$ | SE $b$ | $R^2$ | $F$ |
| 0.416977 | −158.2226 | 0.0349 | 0.0435949 | 0.000216 | 0.9999511 | 40858.03 |
| 0.397121 | −158.0910 | 0.0217 | 0.0426463 | 0.000134 | 0.9999802 | 100796.6 |
| 0.384902 | −158.0437 | 0.0261 | 0.0421925 | 0.000162 | 0.9999706 | 67966.76 |
| 0.374074 | −157.9864 | 0.0403 | 0.0416869 | 0.000250 | 0.9999281 | 27823.07 |
| 0.367069 | −157.9864 | 0.0262 | 0.0415823 | 0.000162 | 0.9999695 | 65571.04 |
| 0.357409 | −157.9623 | 0.0291 | 0.0412865 | 0.000181 | 0.9999617 | 52148.53 |
| 0.302340 | −158.2615 | 0.0407 | 0.0429730 | 0.000252 | 0.9999314 | 29148.5 |
| 0.296957 | −158.2189 | 0.0626 | 0.0429362 | 0.000388 | 0.9998367 | 12244.74 |
| 0.292616 | −158.2825 | 0.0987 | 0.0435092 | 0.000611 | 0.9996065 | 5079.053 |
| 0.281108 | −158.3166 | 0.0967 | 0.0444964 | 0.000599 | 0.9996380 | 5521.748 |
| 0.250814[a] | −157.2813 | 0.2252 | 0.0435598 | 0.001391 | 0.9979679 | 981.1955 |
| 0.231119[b] | −155.5868 | 0.2507 | 0.0410327 | 0.001549 | 0.9971634 | 702.0697 |
| 0.219997[c] | −158.2178 | 0.0721 | 0.0449705 | 0.000461 | 0.9994745 | 9508.927 |
| 0.204998[c] | −158.3317 | 0.1103 | 0.0460226 | .0007297 | 0.9987446 | 3977.803 |

[a] $U = -152.68 - 0.014584T^{3/5} + 0.00018167T^{6/5}$.
[b] $U = -150.44 - 0.023902T^{3/5} + 0.00020213T^{6/5}$.
[c] Additional low-pressure isochors computed specifically to stabilize the EOS analysis. Computed values of $E$, $P$, $T$ are provided in an electronic supplement to this paper.

From Eqs. (18) and (12) the Helmholtz energy may be written

$$A(V,T) = a(V) + T^{3/5}b(V) + \frac{3n}{2}RT - TS(V_0,T_0) - \frac{T}{T_0}\left[a(V) + T_0^{3/5}b(V) - a(V_0) - T_0^{3/5}a(V_0) + \int_{V_0}^{V} P(T_0,V)dV\right] + T\frac{3}{2}\left(\frac{1}{T^{2/5}} - \frac{1}{T_0^{2/5}}\right)b(V) - \frac{3n}{2}RT\ln\left(\frac{T}{T_0}\right) \quad (19)$$

Substitution of Eq. (19) into Eq. (14) gives us the equation of state we seek

$$P(V,T) = \left(\frac{T}{T_0} - 1\right)\frac{da(V)}{dV} + \frac{5}{2}T^{3/5}\left[\left(\frac{T}{T_0}\right)^{2/5} - 1\right]\frac{db(V)}{dV} + \frac{T}{T_0}P(T_0,V) \quad (20)$$

The most important feature of Eq. (20) is the demonstration that a Rosenfeld–Tarazona compatible EOS is an extension of any preferred representation chosen to parameterize $P$–$V$ data along a suitable reference isotherm, i.e. $P(V,T_0)$. One can insert any pressure explicit equation, such as Eq. (1), into Eq. (20) to produce a practical expression. In what follows, we utilize the Universal EOS, which has already been fitted to the 5000 K isotherm (Table 1).

The functions $a(V)$ and $b(V)$ may be obtained by interpolating the regression coefficients of Table 3 as a function of volume (Fig. 8). We have found that an interpolating polynomial is a good representation of $a(V)$ and $b(V)$ as long as additional constraints are imposed on the *slopes* of the interpolants, especially near the upper volume limit. These additional constraints arise because $\frac{da(V)}{dV}$ and $\frac{db(V)}{dV}$ affect the modeled value of the thermal pressure coefficient ($\alpha K$), which is calculated from

$$\alpha K = \left(\frac{\partial P}{\partial T}\right)_V = \frac{1}{T_0}\frac{da(V)}{dV} + \frac{3}{2}T^{-2/5}\left[\frac{5}{3}\left(\frac{T}{T_0}\right)^{2/5} - 1\right] \times \frac{db(V)}{dV} + \frac{P(T_0,V)}{T_0} \quad (21)$$

Eq. (21) is readily derived by differentiation of Eq. (20). As discussed in Part I, the quantity $(\frac{\partial P}{\partial T})_V$ may be estimated directly from MD simulations performed along a given isochore. For the present purposes, we extract an average $P$–$T$ slope for each isochore (Table 4, insert Fig. 8) and use these

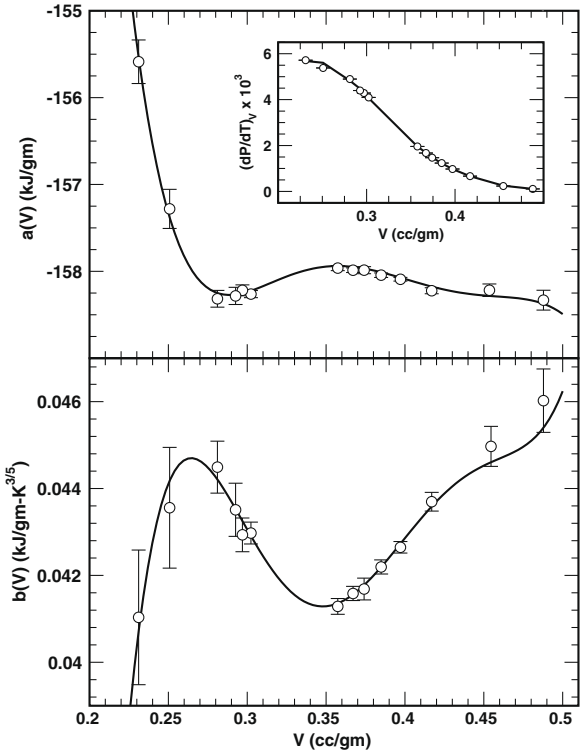


Fig. 8. Variation of the Rosenfeld–Tarazona coefficients of Table 3 and the thermal pressure coefficient (inset; Table 4) with specific volume. Both trends are modeled with 6th degree polynomials, which are plotted; coefficients are reported in Table 5.

Table 4
Estimates of $(\partial P/\partial T)_V$ from MD isochors.

| Volume (g/cm$^3$) | $(\partial P/\partial T)_V$ | SE | $R^2$ |
|---|---|---|---|
| 0.416977 | 57.18 | 0.893 | 0.999 |
| 0.397121 | 53.81 | 1.40 | 0.997 |
| 0.384902 | 48.96 | 0.563 | 0.999 |
| 0.374074 | 43.97 | 0.508 | 0.999 |
| 0.367069 | 42.87 | 0.373 | 1.000 |
| 0.357409 | 40.96 | 0.636 | 0.999 |
| 0.302340 | 19.60 | 0.088 | 1.000 |
| 0.296957 | 16.72 | 0.330 | 0.998 |
| 0.292616 | 14.69 | 0.235 | 0.999 |
| 0.281108 | 12.34 | 0.252 | 0.998 |
| 0.250814 | 9.774 | 0.453 | 0.991 |
| 0.231119 | 6.649 | 0.514 | 0.977 |
| 0.219997 | 2.331 | 0.434 | 0.852 |
| 0.204998 | 1.100 | 0.377 | 0.631 |

Units: GPa/K $\times 10^{-4}$.

slopes as estimates for $(\frac{\partial P}{\partial T})_V$. Polynomial interpolating functions for $a(V)$ and $b(V)$ derived under these constraints are drawn in Fig. 8 and coefficients are reported in Table 5.

Results computed from the Rosenfeld–Tarazona-Universal (RTU) EOS are plotted in Fig. 9 and compared to data from Part I. Two sets of isotherms are indicated, corresponding to the low- and high-$P$ parameterizations of the Universal EOS along the 5000 K reference isotherm ($T_0$). For brevity, we will refer to these as the low-$P$ RTU and high-$P$ RTU, respectively. In Fig. 10, the internal energy computed from Eq. (12) is plotted and compared to data from Part I. As in Fig. 9, two sets of isotherms are indicated. Where a given low-$P$ RTU isotherm intersects the corresponding high-$P$ RTU isotherm in Figs. 9 and 10, the values of $P$, $V$, $E$, and $T$ are identical for both parameterizations. At such a state point the entropy difference between the two models is given from Eq. (18) as

$$\Delta S(V,T) = \Delta S(V_0,T_0) + \frac{1}{T_0}\int_{V_0}^{V}[P_H(T_0,V) - P_L(T_0,V)]dV \tag{22}$$

where the subscript denotes high ($H$) and low ($L$) pressure. As a model parameter, we are free to choose the entropy difference in the reference state $[\Delta S(V_0,T_0)]$ to exactly cancel the volume integral of the reference isotherm EOS, thereby zeroing $\Delta S(V,T)$. Consequently, $S$ can be made identical for both parameterizations at the point where

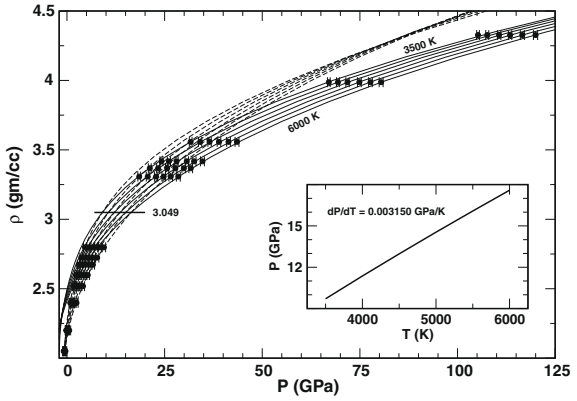


Fig. 9. Modeled densities computed from the RTU EOS and the parameters of Table 5 (5000 K isotherm of Table 1) compared to MD simulation data from Part I. Dashed curves calculated from low-pressure parameterization, solid curves from high-pressure parameterization. Uncertainty in MD pressure estimates is within the size of the symbols. The transition between the low- and high-$P$ structures is indicated by the short horizontal line labeled with the transition density. The $P$–$T$ transition path is plotted in the inset.

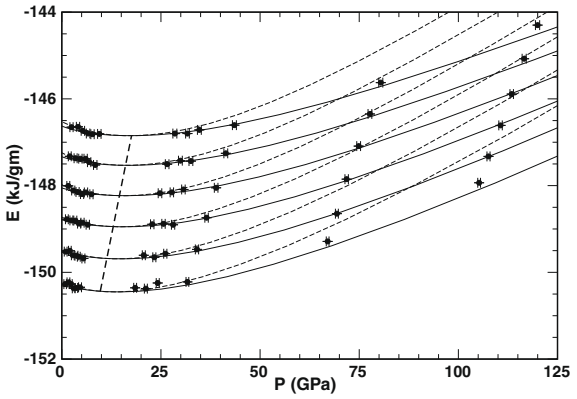


Fig. 10. Internal energies computed from the Rosenfeld–Tarazona model using the parameters of Table 5 compared to MD simulation data from Part I. Uncertainty in MD pressure estimates is within the size of the symbols. The transition between the low- and high-$P$ structures is indicated by the dashed line.

the RTU isotherms cross. Identical values of $V$, $E$, $T$, $P$, and $S$ imply identical values of $A$, the Gibbs free energy ($G$), and the enthalpy ($H$). Formally, this condition can

Table 5
Rosenfeld–Tarazona coefficients.

| $a_0$ | $a_1$ | $a_2$ | $a_3$ | $a_4$ | $a_5$ | $a_6$ |
|---|---|---|---|---|---|---|
| 501.077 | −9323.96 | 53222.6 | −156109 | 246019 | −194390 | 58172.9 |
| $a(V) = a_0 + a_1V + a_2V^2 + a_3V^3 + a_4V^4 + a_5V^5 + a_6V^6$ (kJ/g) | | | | | | |
| $b_0$ | $b_1$ | $b_2$ | $b_3$ | $b_4$ | $b_5$ | $b_6$ |
| −1.81314 | 25.6373 | −137.563 | 355.943 | −433.001 | 167.220 | 49.6361 |
| $b(V) = b_0 + b_1V + b_2V^2 + b_3V^3 + b_4V^4 + b_5V^5 + b_6V^6$ (kJ/g K$^{3/5}$) | | | | | | |

$V$ in cm$^3$/g; the order of the interpolating polynomial is chosen to fit the $a$, $b$, $(\frac{\partial P}{\partial T})_V$ values (Tables 3 and 4) at the estimated level of uncertainty.

be interpreted as one of equilibrium between two "phases," and the locus of isotherm intersections in Fig. 9 can be thought of as the path of a "phase transition." In keeping with the fact that our justification for utilizing a low- and high-$P$ parameterization is driven by apparent changes in melt structure, the modeled "transition" between these two liquids is here determined to be displacive or second order ($\Delta S = 0,\ \Delta V = 0$). Most likely, the "transition" is not strictly univariant as displayed in Fig. 9, but is smeared out over an interval as is typical of most displacive or order–disorder transformations. If we were interested in modeling details of the behavior of the thermodynamic properties in the region of the "transition" a possible procedure might be to introduce an ordering parameter, $0 \leqslant \sigma \leqslant 1$, into the model and rewrite Eq. (19) as

$$\begin{aligned} A(V,T) = {} & a(V) + T^{3/5} b(V) + \frac{3n}{2} RT - TS(V_0, T_0) \\ & - \frac{T}{T_0}\left\{ a(V) + T_0^{3/5} b(V) - a(V_0) - T_0^{3/5} b(V_0) \right. \\ & \left. + \int_{V_0}^{V} [\sigma P_L(T_0, V) + (1-\sigma) P_H(T_0, V)] dV \right\} \\ & + T \frac{3}{2} \left( \frac{1}{T^{2/5}} - \frac{1}{T_0^{2/5}} \right) b(V) - \frac{3n}{2} RT \ln\left(\frac{T}{T_0}\right) + RT\Omega(\sigma) \end{aligned} \tag{23}$$

where $\Omega(\sigma)$ [$\lim_{\sigma \to 0,1} \Omega(\sigma) = 0$] is a function that describes the mixing entropy across the transition. In Eq. (23) a zero value of $\sigma$ would utilize the high-$P$ parameterization, while a value of unity would utilize the low-$P$ calibration. Intermediate values of $\sigma$ are determined by minimizing $A$ with respect to $\sigma$, i.e. imposing the condition of *homogeneous* equilibrium [set $(\frac{\partial A}{\partial \sigma})_{V,T} = 0$ and solve for $\sigma$]. As our interests are not focused on the details of the "transition" interval, we will leave the development of the order parameter extension of RTU to a subsequent paper and more appropriate data set.

The modeled thermal pressure coefficient is plotted in Fig. 11a. Comparison should be drawn with results from the alternative EOS plotted in Fig. 6a. Both models of the thermal pressure coefficient represent the data set in a statistically equivalent manner, but the functional form of the RTU EOS is clearly superior in transitioning between the low- and high-$P$ regimes.

In Fig. 11b, the isochoric heat capacity, which is given by

$$C_V = \frac{3}{5} \frac{b(V)}{T^{2/5}} + \frac{3n}{2} R \tag{24}$$

from the Rosenfeld–Tarazona model of the internal energy (Eq. (12)), is plotted and compared to MD estimates. Results plotted in Fig. 11b should be compared to those in Fig. 6b. The RTU model is better at reproducing the $C_V$ estimates, as might be expected given the number of parameters devoted in the RTU model to the temperature-dependence of the internal energy. Nevertheless, as with the thermal pressure coefficient, the transition between the low- and high-$P$ regimes is better modeled by the RTU formalism.

Model expressions for the bulk modulus and for the isobaric coefficient of thermal expansion are given by

$$\begin{aligned} K = {} & -\left(\frac{T}{T_0} - 1\right) V \frac{d^2 a(V)}{dV^2} - \frac{5}{2} T^{3/5} \left[ \left(\frac{T}{T_0}\right)^{2/5} - 1 \right] V \\ & \times \frac{d^2 b(V)}{dV^2} - \frac{T}{T_0} V \frac{dP(T_0, V)}{dV} \end{aligned} \tag{25}$$

and

$$\alpha = -\frac{\frac{1}{T_0}\frac{da(V)}{dV} + \frac{3}{2} T^{-2/5} \left[ \frac{5}{3} \left(\frac{T}{T_0}\right)^{2/5} - 1 \right] \frac{db(V)}{dV} + \frac{P(T_0,V)}{T_0}}{V \left\{ \left(\frac{T}{T_0} - 1\right) \frac{d^2 a(V)}{dV^2} + \frac{5}{2} T^{3/5} \left[ \left(\frac{T}{T_0}\right)^{2/5} - 1 \right] \frac{d^2 b(V)}{dV^2} + \frac{T}{T_0} \frac{dP(T_0,V)}{dV} \right\}} \tag{26}$$

These quantities, along with the thermal Grüneisen parameter, are plotted in Fig. 11c–e. Compare these results with those of the alternate model plotted in Fig. 6c–e.

The RTU EOS model of the isothermal bulk modulus is clearly superior to the volume-explicit EOS of Eq. (3). While fits to the low-pressure isochors are statistically equivalent in both models, data recovery is much better for the RTU equation at higher pressures. Modeled values of $\alpha$ and $\gamma$ from the RTU EOS also reproduce the MD array with smaller systematic residuals.

In summary, we find that the RTU model is preferable in representing the thermodynamic properties of $CaAl_2Si_2O_8$ liquid as computed by the molecular dynamics study of Part I. The temperature-dependent Universal EOS (Eq. (2)) does not capture the correct functional form of the $V$–$T$–$P$ relations. The volume-explicit EOS of Ghiorso (2004a) (Eq. (3)) does a much better job over the Universal equation at representing the data array, and does so with a minimal number of adjustable parameters. We prefer the RTU formulation because there are fewer systematic offsets to model residuals compared to the Ghiorso equation and because the temperature-dependence of the model is rooted in physical theory. In applying the model developed here, it should be borne in mind that the potential energy–temperature relation of Rosenfeld and Tarazona (1998) does fail at very high-pressure, and model predictions at $P > 70$ GPa should be questioned. We recommend that the model not be applied much outside the density range 2.2–4.3 g/cc, as extrapolation of the functions $a(V)$ and $b(V)$ might potentially give erroneous results. Extrapolation in temperature is much more secure. We recommend that the low-$P$ RTU model be used up to the "transition" curve (Fig. 9) and the high-$P$ model be used for denser fluids. As the "transition" is modeled as second order, there will be no discontinuities in *G, A, E, H, S*, or $V$ as a consequence of this approximation.

## 4. APPLICATIONS OF THE MODEL

In this section we will apply our thermodynamic model to calculation of the liquid–liquid first order phase transition and shock Hugoniot of molten $CaAl_2Si_2O_8$ and compare the latter to experimental results.

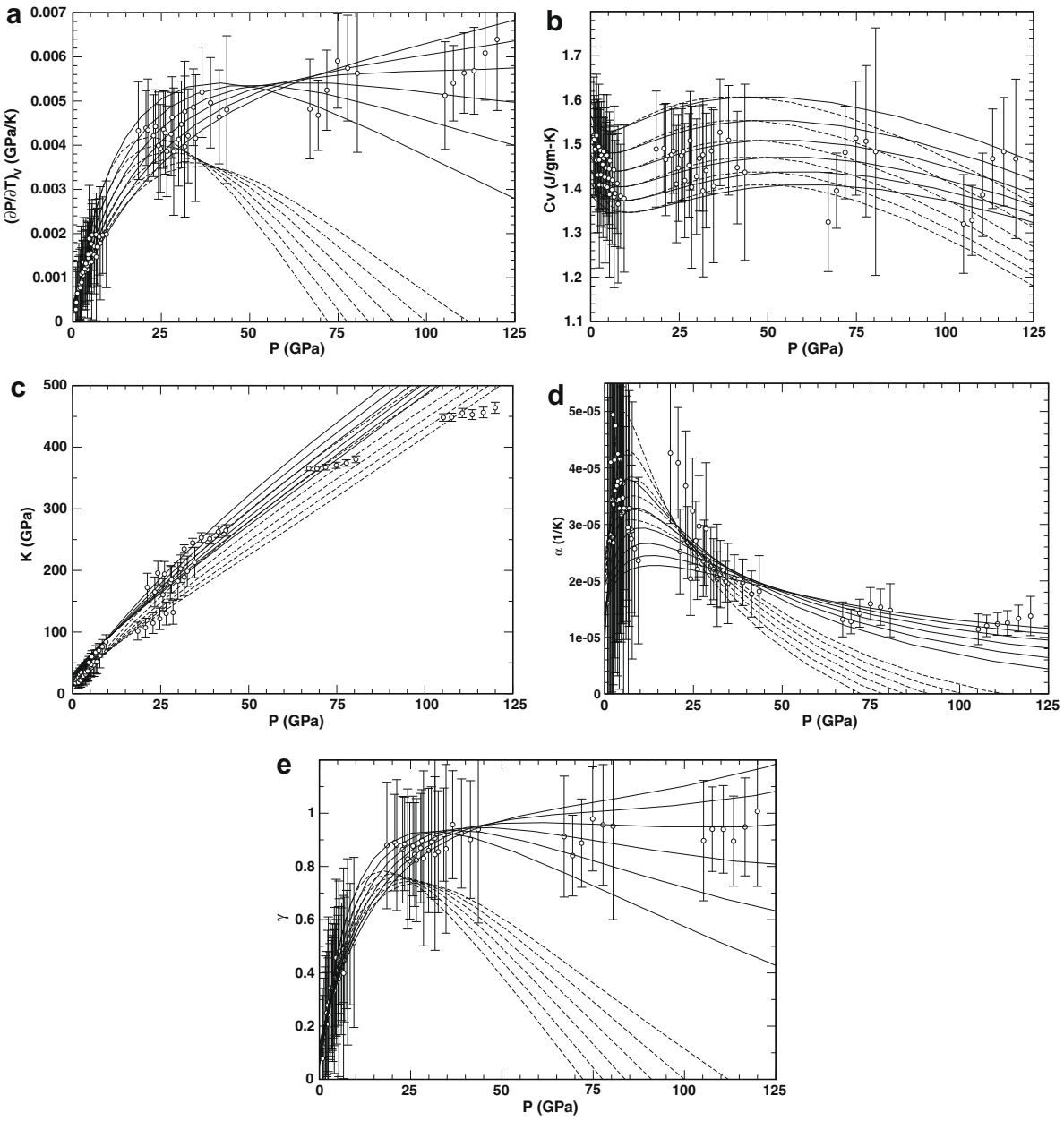


Fig. 11. Modeled derivative properties computed from the RTU EOS and the parameters of Table 5 (5000 K isotherm of Table 1) compared to MD simulation data from Part I. Dashed curves calculated from low-pressure parameterization, solid curves from high-pressure parameterization. Uncertainty in MD derived quantities is shown as $\pm 1\sigma$. (a) Thermal pressure coefficient, equivalent to $\alpha K$. (b) Isochoric heat capacity. (c) Bulk modulus. (d) Isobaric thermal coefficient of expansion. (e) Thermal Grüneisen coefficient.

### 4.1. Liquid–liquid phase transition

A criterion for the thermodynamic stability of a phase is that its bulk modulus is a positive quantity. Modeled $P$–$V$–$T$ state points for which the bulk modulus is negative violate this stability condition; a single homogeneous phase cannot exist at these state points. The onset of instability corresponds to the locus of $P$–$V$–$T$ points which satisfy the EOS of the substance and which zero the bulk modulus ($(\frac{\partial P}{\partial V})_T = 0$, Prigogene and Defay, 1954). In a muliticomponent system, un-mixing into two phases generally results in differential partitioning of components. In a single component system however, coexisting phases differ in structure (density) rather than composition. In the case of the RTU EOS model of $CaAl_2Si_2O_8$ liquid described in the previous section, the incipient instability condition is given by (from Eq. (20))

$$0 = -\left(\frac{T}{T_0} - 1\right)\frac{d^2a(V)}{dV^2} - \frac{5}{2}T^{3/5}\left[\left(\frac{T}{T_0}\right)^{2/5} - 1\right]\frac{d^2b(V)}{dV^2} - \frac{T}{T_0}\frac{dP(T_0,V)}{dV} \qquad (27)$$

In the literature on liquid–liquid phase transitions in single component fluids, the $V$–$T$ curve resulting from solution of an equation like Eq. (27) is often referred to as the spinodal curve (e.g. Saika-Voivod et al., 2000), which is strictly a misnomer, as spinodal should be applied to the limit of compositional stability at fixed $T$ and $P$ in a multicomponent system. Nevertheless, we will also refer to this curve as the spinode.

The spinode calculated from Eq. (27) using our RTU model parameterization of $CaAl_2Si_2O_8$ liquid is plotted in Fig. 12 as the heavy solid curves. The state point labeled alternately $\rho_C$, $T_C$, and $P_C$ in the figure is the critical point corresponding to the onset of un-mixing. This is the highest temperature point for which a solution of Eq. (27) may be found. In the two plots on the left panel of the figure, $P$–$T$ and $T$–$\rho$ projections of the spinodal curve are shown with the unstable region ($K < 0$) shaded. Note, that these projections should not be interpreted as phase diagrams, as the limbs of the curves do not necessarily define coexisting compositions in mechanical equilibrium, e.g. in the $T$–$\rho$ plot the limbs of the spinodal curve are at different pressures. To explore the limits of equilibrium un-mixing attention should be focused on the diagram in the right panel of the figure. Here the spinode is shown along with isotherms (dashed curves) that give solutions to the RTU EOS in $P$–$\rho$ space. An isotherm with multiple values of $\rho$ for a given $P$ brackets a region of un-mixing, with the densities of equilibrium coexisting liquids being given by the minimum and maximum densities along that isotherm. The heavy dashed curve corresponds to the critical isotherm, above which all liquids are stable. At temperatures below the critical isotherm, ($P$, $\rho$) points that plot interior to the limbs of the spinode characterize unstable liquids that undergo spontaneous un-mixing. Those that plot exterior to the spinode but within the two-phase region are metastable liquids, whose un-mixing may be kinetically inhibited. The heavy dotted curve indicates the maximum extent of the equilibrium two-phase region for higher density liquids.

The modeled critical point is well above the temperature of the glass transition (Morgan and Spera, 2001a,b) but below the liquid field in the liquid–solid phase diagram modeled by Ghiorso (2004b). Comparing the critical density to densities plotted in Fig. 1, it can be seen that the onset of un-mixing corresponds to a liquid with average coordination number of $SiO^{[5]}$. Un-mixing leads to coexisting liquids with higher and lower Si-coordination states, and it may be important to note that the break in slope of the $V$–$SiO^{[\bar{n}]}$ relations plotted in Fig. 1 corresponds approximately to the critical density. Perhaps the "phase transition" that we discuss above between the low- and high-$P$ structures is a high-temperature manifestation of the same positive enthalpic drive that generates the low-temperature liquid–liquid immiscibility?

Experimental verification of this model prediction of liquid–liquid un-mixing would necessitate X-ray or optical observations of phases of differing density in supercooled $CaAl_2Si_2O_8$-composition liquids. Optical measurements by Kuryaeva (2006) and Raman studies by Le Parc et al. (2003) do not report evidence for un-mixing, but both studies used material prepared by rapid quenching from the liquid state at room pressure. To have any hope of detecting the two-phase region, samples would have to be annealed below $T_C$, but this temperature is too low at ambient pressure (Fig. 12) to overcome kinetic barriers to phase separation at laboratory time scales. Supercooled liquids annealed at higher pressures and temperatures (~1.5 GPa and ~1500 K, i.e. Fig. 12) would be ideal candidates for examination, but we are not aware of experimental studies of material prepared under these conditions.

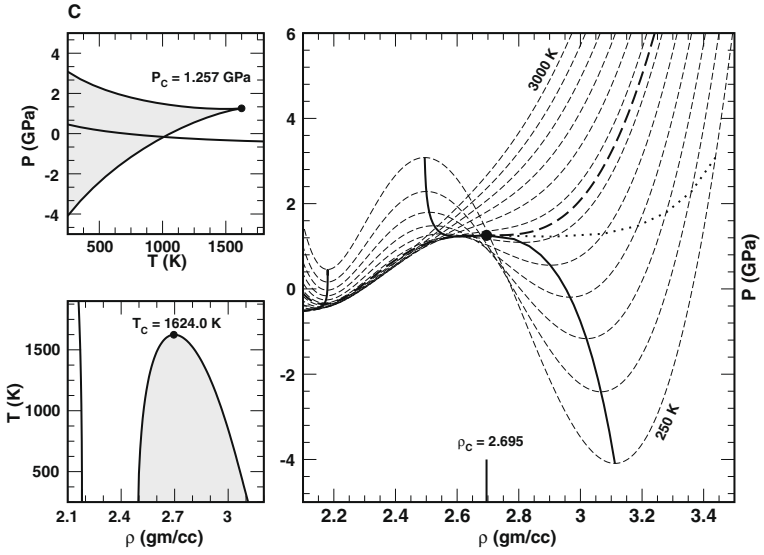


Fig. 12. Modeled spinodal curve computed from the RTU EOS and the parameters of Table 5 (5000 K isotherm of Table 1). The critical temperature ($T_C$), pressure ($P_C$), and density ($\rho_C$) are indicated. Model isotherms are plotted in the right panel and indicated by the dashed curves; the heavy dashed curve is the critical isotherm. The dotted curve indicates the limit of the two-phase field.

### 4.2. Calculation of the shock wave Hugoniot

An experimentally determined shock wave Hugoniot for $CaAl_2Si_2O_8$ liquid is reported by Rigden et al. (1989). The data of Rigden et al. (1989) are complemented by the more recent and higher pressure shock wave experiments of Asimow and Ahrens (2008). Both data sets are interesting in that they indicate fairly extreme levels of compression at moderate- to high-pressure, in contrast to the MD simulation data of Part I. In this context, we compare these experimental data to the Hugoniot calculated from the RTU EOS developed above.

The model Hugoniot is a univariant curve in $P$–$V$–$T$ space computed by satisfying simultaneously an EOS, and an energy balance equation (e.g. Ghiorso, 2004b, his Eq. (4))

$$E - E_i = \frac{1}{2}(P - P_i)(V_i - V) \tag{28}$$

where $E$ is the specific internal energy and the subscript $i$ denotes the *initial* conditions of the shock. Eq. (28) may be easily expressed in a form compatible with the RTU model. Substituting Eqs. (12) and (20) into Eq. (28) gives

$$\begin{aligned} a(V) - a(V_i) + T^{3/5}\left[b(V) - \left(\frac{T_i}{T}\right)^{3/5} b(V_i)\right] + \frac{3n}{2}\frac{R(T - T_i)}{M} \\ = \frac{1}{2}\left\{\left(\frac{T}{T_0} - 1\right)\frac{da(V)}{dV} + \frac{5}{2}T^{3/5}\left[\left(\frac{T}{T_0}\right)^{2/5} - 1\right]\frac{db(V)}{dV} \right. \\ \left. + \frac{T}{T_0}P(T_0, V)\right\}(V_i - V) - \frac{1}{2}\left\{\left(\frac{T_i}{T_0} - 1\right)\frac{da(V_i)}{dV} \right. \\ \left. + \frac{5}{2}T_i^{3/5}\left[\left(\frac{T_i}{T_0}\right)^{2/5} - 1\right]\frac{db(V_i)}{dV} + \frac{T_i}{T_0}P(T_0, V_i)\right\}(V_i - V) \end{aligned} \tag{29}$$

Taking initial conditions from Rigden et al. (1989, $T_i = 1923$ K, $P_i = 0.0001$ GPa, and $V_i = 0.406593$ cm$^3$/g, RTU EOS low-$P$), the model Hugoniot is computed by simultaneous solution of Eqs. (20) and (29). Results are plotted in Fig. 13 along with experimental data. Also shown are model $\rho$–$P$ isotherms and experimental data describing the Hugoniot of pressure-amorphized (Campbell and Heinz, 1993), initially crystalline-anorthite ($CaAl_2Si_2O_8$) from Jeanloz and Ahrens (1980) and anorthite glass from Boslough et al. (1986).

It is apparent that the model curve is inconsistent with the experimental data of Rigden et al. (1989) and Asimow and Ahrens (2008). Even if the model isotherms are systematically displaced by ~0.1 g/cc to accommodate the lowest pressure data and to bring the MD densities into agreement with Rigden et al.'s (1989) *estimate* of the initial density, the six highest pressure points will not fall along an isotherm that is consistent with the internal energy constraint. The principal reason the model Hugoniot differs from the experimental one is because the model $\rho$–$P$ isotherms steepen rapidly with increasing pressure, reflecting a significantly larger bulk modulus at pressure. The zero pressure $K$ modeled by Rigden et al. (1989) is ~20 GPa, which is in excellent agreement with the quantity estimated from sound speed measurements (Ai and Lange, 2008) and in good

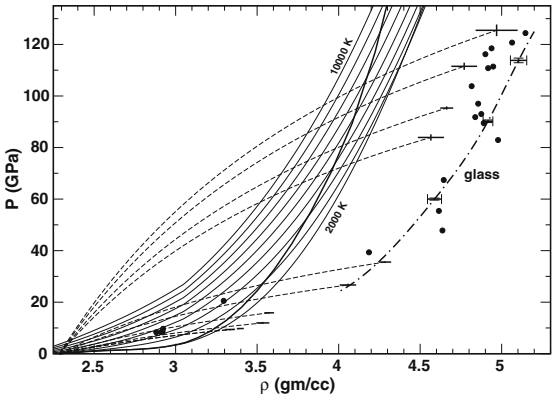


Fig. 13. Modeled Hugoniot (solid curve) computed from the RTU EOS and the parameters of Table 5 (5000 K isotherm of Table 1) compared to experimental data from Rigden et al. (1989) on shocked liquid (six lowest pressure brackets), Asimow and Ahrens (2008) on shocked liquid (four highest pressure brackets), Jeanloz and Ahrens (1980) on shocked crystalline anorthite (three pressure brackets connected by the dashed-dot Hugoniot curve), and Boslough et al. (1986) on shocked glass (filled circles). The dashed curves are Rayleigh lines connecting initial and final shock states. EOS isotherms are shown as solid lines and are spaced every 1000 K.

agreement with the RTU EOS model value (Fig. 11c; ~10 GPa at zero pressure, ~20 GPa at a pressure of 1.5 GPa). However, the Hugoniot datum at ~40 GPa requires ~40% compression, which yields an average $K$ of ~75 GPa; that at 80 GPa a compression of ~45%, which yields an average $K$ of ~130; and that at 125 GPa a compression of 50%, which yields an average $K$ of ~180. All these values are a factor of two to three lower than the MD data permit. This discrepancy between the modeled and experimental Hugoniot may indicate that the MD results of Part I significantly underestimate the density of the liquid by as much as ~10% at pressures greater than 30 GPa. Alternatively, the comparison may indicate that the experimental work, especially at the highest pressures, does not reflect the properties of a liquid.

The two highest-pressure experimental points of Rigden et al (1989) along the liquid Hugoniot intersect the curve of Jeanloz and Ahrens (1980) that corresponds to their shock wave measurements on single crystal anorthite (Fig. 13, brackets connected by the dashed-dot curve). The data of Jeanloz and Ahrens are now interpreted (Campbell and Heinz, 1993) to reflect the properties of an amorphized substance and this conclusion along with the data of Boslough et al. (1986; solid circles in Fig. 13) leads to the observation that the experimentally determined densities of the liquid and of the glass are identical at pressures in the interval 25–40 GPa. Given that the shock temperatures of the liquid are likely higher than those of the solid (Rigden et al., 1989, estimate ~2200 K, while Jeanloz and Ahrens, 1980, estimate ~1500 K at 40 GPa), the implication is that a density crossover of the liquid relative to the glass occurs at pressures on the order of 20 GPa. While not implausible, this seems unlikely. One possible speculation is that the highest $P$ data of Rigden et al. (1989) correspond to glass and not to liquid. On the other hand, the data of Asimow and

Ahrens (2008) plot at lower densities than the glass data at comparable pressures, and the interpretation of the final shock state of these experiments as anything other than liquid would be purely speculative. A numerical experiment can be performed to test the notion that a phase transition would shift the modeled Hugoniot to higher densities thereby reconciling the MD results with experimental observation. A first order transition at ~20 GPa involving an internal energy change of ~10 kJ/g would be sufficient to bring the modeled Hugoniot into agreement with observation, but energies of this magnitude are characteristic of liquid–gas phase transitions and not those of condensed phases. Consequently, reconciliation of the MD modeled Hugoniot with experiment cannot readily be ascribed to any solid–liquid or liquid–liquid phase transition. The most likely explanation of the discrepancy between our modeled Hugoniot and the experimental one is that the MD results of Part I under predict the density of the liquid by about 10% at pressures greater than ~20 GPa. New MD simulations for liquid $CaAl_2Si_2O_8$ using the transferable potential of Matsui (1998) are currently underway and will be used to reexamine this issue.

## 5. SUMMARY

A thermodynamic model is developed for $CaAl_2Si_2O_8$ liquid that successfully parameterizes the molecular dynamics data set of Part I. The model is based upon the isothermal Universal EOS (Vinet et al., 1986) combined with an expression for the temperature-dependence of the internal energy derived from density functional theory (Rosenfeld and Tarazona, 1998). This model is more successful at reproducing the data than the extended Universal EOS (Vinet et al., 1987) or the volume-explicit EOS of Ghiorso (2004a). The data of Part I require separate parameterizations of low (<20 GPa) and high (>20 GPa) pressure regimes, which we interpret as having distinctly different liquid structures. The transition between these two regimes is modeled as second order, although the nature of the transition is open to question and may well be first order or lambda-like in character.

Our thermodynamic model predicts a region of liquid–liquid un-mixing at low-temperatures and pressures.

A shock wave Hugoniot curve is calculated for comparison with the experimental data of Rigden et al. (1989) and of Asimow and Ahrens (2008). The comparison is unfavorable and we conclude that most likely the MD data of Part I underestimates the density of the liquid by roughly 10% at pressures greater than 20 GPa.

While the EOS formalism and analysis techniques developed in this paper should be applicable to a wide range of silicate liquid bulk compositions, the parameterization developed here for $CaAl_2Si_2O_8$ liquid is likely not applicable to naturally occurring melts. The abundance of $(Si,Al)O^{[5]}$ at very low pressure (Part I) and the observation that the shift from a liquid dominated by $(Si,Al)O^{[4]}$ to $(Si,Al)O^{[5]}$ to $(Si,Al)O^{[6]}$ takes place at lower pressures than other silicate liquids makes $CaAl_2Si_2O_8$ liquid unusual (see Ghiorso, 2004b, for a summary of MD results pertaining to this issue). We suspect that these low-pressure coordination shifts generate positive enthalpic contributions that drive liquid–liquid un-mixing to higher temperatures, whereas in a more typical liquid, like molten $Mg_2SiO_4$, where the cation coordination shifts take place at much higher pressures, the enthalpic contributions are less influential, and consequently, the critical temperature is well below the glass transition (Martin et al., 2009). The unusual characteristics of molten $CaAl_2Si_2O_8$ makes it an interesting liquid to study but at the same time renders inferences drawn from its physical properties problematic when applied to melting in silicate planetary bodies.

## ACKNOWLEDGMENTS

We are indebted to Pascal Richet for his insightful review and for making us aware of the important references on Ar-solubility by Bouhifd and coworkers. We acknowledge the thoughtful attention of three anonymous reviewers whose suggestions helped improve the manuscript. Material support for this investigation was provided by grants from the National Science Foundation to MG (EAR-0608532). This is contribution #13 of OFM-Research, Inc.

## REFERENCES

Ai Y. and Lange R. A. (2008) New acoustic velocity measurements on CaO–MgO–$Al_2O_3$–$SiO_2$ liquids: reevaluation of the volume and compressibility of $CaMgSi_2O_6$–$CaAl_2Si_2O_8$ liquids to 25 GPa. *J. Geophys. Res. Solid Earth* **113**, B04203. doi:10.1029/2007JB005010.

Asimow P. D. and Ahrens T. J. (2008) Shock compression of liquid silicates to 125 GPa: the anorthite-diopside join. *Eos Transactions, AGU*, **89**(53), *Fall Meeting Supplement*. #MR32B-04 (abstr.).

Bevington P. R. (1969) *Data Reduction and Error Analysis for the Physical Sciences*. McGraw Hill, New York, p. 336.

Boslough M. B., Rigden S. M. and Ahrens T. J. (1986) Hugoniot equation of state of anorthite glass and lunar anorthosite. *Geophys. J. Roy. Astr. Soc.* **84**, 455–473.

Bouhifd M. A. and Jephcoat A. P. (2006) Aluminum control of argon solubility in silicate melts under pressure. *Nature* **439**, 961–964.

Bouhifd M. A., Jephcoat A. P. and Kelley S. P. (2008) Argon solubility drop in silicate melts at high pressures: a review of recent experiments. *Chem. Geol.* **256**, 252–258.

Campbell A. and Heinz D. (1993) An amorphous phase on the anorthite Hugoniot. *Geophys. Res. Lett.* **20**, 237–240.

Flory P. J. (1988) *Statistical Mechanics of Chain Molecules*. Hanser Publishers, New York, p. 432.

Ghiorso M. S. (2004a) An equation of state for silicate melts. I. Formulation of a general model. *Am. J. Sci.* **304**, 637–678.

Ghiorso M. S. (2004b) An equation of state for silicate melts. III. Analysis of stoichiometric liquids at elevated pressure: shock compression data, molecular dynamics simulations and mineral fusion curves. *Am. J. Sci.* **304**, 752–810.

Ghiorso M. S. and Kress V. C. (2004) An equation of state for silicate melts. II. Calibration of volumetric properties at 105 Pa. *Am. J. Sci.* **304**, 679–751.

Jeanloz R. and Ahrens T. J. (1980) Anorthite: thermal equation of state to high pressures. *Geophys. J. Roy. Astr. Soc.* **62**, 529–549.

Kuryaeva R. (2006) Degree of polymerization of the $CaAl_2Si_2O_8$ aluminosilicate glass. *Glass Phys. Chem.* **32**, 505–510.

Lange R. A. and Navrotsky A. (1992) Heat capacities of $Fe_2O_3$-bearing silicate liquids. *Contrib. Mineral. Petrol.* **110**, 311–320.

Le Parc R., Champagnon B., Dianoux J., Jarry P. and Martinez V. (2003) Anorthite and $CaAl_2Si_2O_8$ glass: low frequency Raman spectroscopy and neutron scattering. *J. Non-Crystalline Solids* **323**, 155–161.

Martin G. B., Spera F. J., Ghiorso M. S. and Nevins D. (2009) Structure, thermodynamic, and transport properties of molten $Mg_2SiO_4$: molecular dynamics simulations and model EOS. *Am. Mineralogist* **94**, 693–703.

Matsui M. (1998) Computational modeling of crystals and liquids in the system $Na_2O$–CaO–MgO–$Al_2O_3$–$SiO_2$. In *Properties of Earth and Planetary Materials at High Pressure and Temperature* (eds. M. H. Manghanni and T. Yagi). American Geophysical Union, Washington, DC, pp. 145–148.

Morgan N. A. and Spera F. J. (2001a) Glass transition, structural relaxation, and theories of viscosity: a molecular dynamics study of amorphous $CaAl_2Si_2O_8$. *Geochim. Cosmochim. Acta* **65**, 4019–4041.

Morgan N. A. and Spera F. J. (2001b) A molecular dynamics study of the glass transition in $CaAl_2Si_2O_8$: thermodynamics and tracer diffusion. *Am. Mineral.* **86**, 915–926.

Prigogene I. and Defay R. (1954) *Chemical Thermodynamics*. Longmans Green and Co., New York, p. 543.

Rigden S. M., Ahrens T. J. and Stolper E. M. (1989) High-pressure equation of state of molten anorthite and diopside. *J. Geophys. Res.* **94**, 9508–9522.

Rosenfeld Y. and Tarazona P. (1998) Density functional theory and the asymptotic high density expansion of the free energy of classical solids and fluids. *Mol. Phys.* **95**, 141–150.

Saika-Voivod I., Sciortino F. and Poole P. H. (2000) Computer simulations of liquid silica: equation of state and liquid–liquid phase transition. *Phys. Rev. E* **63**, 011202.

Spera F. J., Nevins D., Cutler I. and Ghiorso M. S. (2009) Structure, thermodynamic and transport properties of $CaAl_2Si_2O_8$ liquid: Part I. Molecular dynamics simulations. *Geochim. Cosmochim. Acta* **73**, 6918–6936.

Thompson, Jr., J. B. (1969) Chemical reactions in crystals. *Am. Mineral.* **54**, 341–375.

Thompson, Jr., J. B. (1970) Chemical reactions in crystals: Corrections and clarification. *Am. Mineral.* **55**, 528–532.

Tolédano J.-C. and Tolédano P. (1987) *The Landau Theory of Phase Transitions*. World Scientific Lecture Notes in Physics, vol. 3, p. 451.

Vinet P., Ferrante J., Smith J. R. and Rose J. H. (1986) A universal equation of state for solids. *J. Phys. C. Solid State Phys.* **19**, L467–L473.

Vinet P., Rose J. H., Ferrante J. and Smith J. R. (1989) Universal features of the equation of state of solids. *J. Phys. Condens. Matter* **1**, 1941–1963.

Vinet P., Smith J. R., Ferrante J. and Rose J. H. (1987) Temperature effects on the universal equation of state of solids. *Phys. Rev. B* **35**, 1945–1953.

*Associate editor:* Kelly Russell